

Microstructure and properties characterization of a Ti-Nb high strength micro alloyed steel for cold forming

Bruno Bastos da Silva Murad¹ 
Angelo Fernando Padilha^{2*} 

Abstract

Driven by new market demands, environmental regulations and an ever-increasing pressure for lower weight and carbon footprint reduction in vehicles and transportation industry, suppliers have been pushed to develop new solutions which often translate themselves into more resistant, thinner, and wider hot and cold rolled steel products for downstream forming. In such applications, cracking during flanging operations is the major restriction in the use of an advanced high strength steels and a good stretch-flangeability is an essential property for complex press formed parts such as chassis, suspension arms, semi-trailers, and agricultural components. This paper consists of a wide and logical microstructural and properties characterization of a hot rolled Ti-Nb micro alloyed steel for cold forming, whose simulations via ThermoCalc predicted a final BCC structure with small amounts of cementite with additional FCC carbides. CCT and TTT diagrams also simulated via JMatPro suggested a final microstructure of ferrite α , what was later confirmed by X ray diffraction. Both optical and scanning electronic microscopy confirmed the presence of ferrite α , cementite, and the niobium and/or titanium enriched precipitates predicted in earlier simulations. Finally, yield and tensile strengths of 790 and 815 MPa, respectively, in longitudinal direction, and total elongation until fracture of 17% plus the absence of cracks in bending tests confirmed that sampled material meets all requirements for grades S650MC and S700MC stated in EN1019-2.

Keywords: Hot rolling; Cold forming; High strength low alloy steels.

1 Introduction

High strength steels (HSS) are structural steels characterized by nominal yielding strengths exceeding 460 MPa and its use in construction fields provides higher strength-to-weight ratios and lower material costs when compared with mild steel sections and resulting in their extensive utilization, as evidenced by the growing number of notable architectural projects [1,2].

Yin et al. [2] provide a vast reference list regarding studies on a wide range of steel grades (i.e. from S460 up to S1100), manufacturing routes and sectional shapes (i.e. I-sections, rectangular and circular hollow sections, open sections) and loading scenarios (cross-sections under compression bending and combined compression plus bending).

In the transportation and load handling industry, during the last years, huge efforts have been deployed by suppliers to develop new steel solutions aiming safer, lighter, and more energetically efficient vehicles. It has been shown that lighter cars directly contribute to the reduction of fuel consumption; a 100 kg – reduction in weight corresponds to an 8% improvement in fuel mileage [3]. More severe environmental regulations demanding a reduction of carbon footprint have also acted as driving force to develop more sustainable products and this often translates itself into hot

rolled HSS in wider and thinner dimensions [4-7] aiming higher performance.

Among many manufacturing methods, cold-formed steel sections are light-weight structural members made by bending, pressing, or rolling flat plane sheets at ambient temperature (way below the recrystallization temperature of steels) into different and even complex shapes with relatively low operational and/or capital expenditure [8,9].

Structural components of vehicles, cranes and load trailers may be cold formed and require high mechanical properties associated to good toughness and weldability, such as EN10149-2 S700MC grade. The produced shapes are thin-walled, and the cold-formed members offer one of the highest load capacity-to-weight ratio among the various structural component. [4,6].

The alloying approach (Nb, Ti and V) combined with a specific rolling schedule contributes to strength via precipitation hardening and grain refinement in slab reheating and hot rolling [6,7,10,11]. Simultaneously, recrystallization and recovery phenomena occurring during hot rolling are important because they affect the final properties of products and – industrially important – alter rolling loads. These factors are crucial for obtaining uniform final microstructures and consistency of dimensions and shape of hot rolled steel

^{1,2}Departamento de Engenharia Metalúrgica e de Materiais, Universidade de São Paulo, São Paulo, SP, Brasil.

*Corresponding author: padilha@usp.br



products. Such precision may be achieved by mastering and avoiding dynamic recrystallization of austenite during hot rolling passes and static recrystallization between them and before cooling [4,12]. Also, elements in solid solution (such as manganese and silicon), thermo-mechanical controlled processes and high dislocation densities enhance mechanical properties without compromising other desired properties [5,6,13].

This paper consists of the microstructural and properties characterization of an industrial 2 mm hot rolled Ti-Nb micro alloyed steel for cold forming by combining different and complementary techniques in a broad and logical sequence to provide proper knowledge of the steel subject. The final microstructure predicted by using ThermoCalc and JMatPro softwares was compared to the actual one assessed by both optical and scanning electronic microscopy and by X ray diffraction. Mechanical properties (yield and tensile strengths, total elongation) were also measured and, finally, bending and hole expansion tests were performed to evaluate its ductility.

2 Materials and methods

2.1 Chemical analysis

The chemical composition of the slab was assessed by optical emission spectroscopy (OES) accordingly to ASTM E415-21. The equipment used was ARL OES 4460 supplied by Thermo Fisher Scientific and the sample was obtained from the casting tundish. Table 1 presents the chemical composition of the slab in weight percent.

2.2 Hot rolling

The steel slab (225 x 1520 x 8610 mm) was heated in the furnace from room temperature (approximately 25 °C) up to 1250 °C for approximately 3 hours. After that, it was rolled at the roughing mill to reduce its thickness up to a 30 mm- transfer bar which was coiled in the Coil Box to reduce thermal losses and provide higher uniformity and temperature. In the next step, the transfer bar was rolled in

the 6-stand Finishing Mill up to a nominal 2.0 mm thickness strip, representing a total reduction of approximately 99%.

The strip was finally cooled in the run-out table by a laminar water flow and coiled in the down coiler. After air cooling, the coil was taken to the coil dividing line to collect samples from half length of the coil. Figure 1 represents a schematic layout of the hot strip mill in which the coil was produced.

2.3 Offline simulations

Based on the actual chemical composition of the slab, the ThermoCalc software (version 2018b) with TCFE9 database was used to predict the final microstructure in the strip. As an initial setup, carbon phases such as diamond, graphite and gases were excluded since the main target was to study the iron – cementite system. Also, the system was set for 100 grams to provide direct percent results. At last, temperature was set between 500 and 1600 °C with 50 °C steps.

Continuous Cooling Transformation (CCT) and Temperature – Time – Transformation (TTT) diagrams were simulated by using JMatPro (version 14) with General Steel database.

2.4 Microstructural characterization

2.4.1 Optical and scanning electronic microscopy

Microstructure were submitted to both optical and scanning electronic microscopy (SEM) with additional evaluation by electron backscatter diffraction (EBSD) and energy-dispersive X-ray spectroscopy (EDS) [14].

The optical microscope used was an Axio Imager M2m from Carl Zeiss, with magnification of 200, 400 and 1000 times and an attached camera for image acquisition. On the other hand, the electronic microscope was a field emission gun (FEG) from JEOL, model JSM 7100F.

For optical microscopy, samples from longitudinal (rolling) direction were selected and its edges carefully trimmed by using a silicon carbide disk to eliminate cold working during blanking in the hydraulic guillotine. Then, the samples were embedded in a conductive phenolic resin

Table 1. Chemical composition (in wt.%)

C	Mn	Si	Nb	V	Ti	Mo	B	N
< 0.080	< 1.800	< 0.300	< 0.055	< 0.010	< 0.150	< 0.10	< 0.001	< 0.005

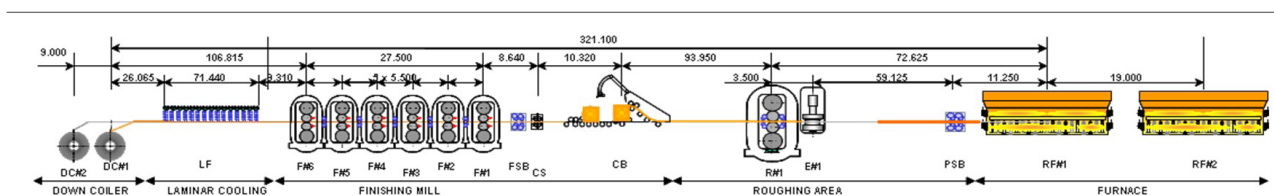


Figure 1. Schematic layout of the hot strip mill in which the coil was rolled

with carbon addition. The embedded samples were initially ground in an automatic machine, following the sequence of diamond sandpaper grid of 120, 220, 500 and 1200 until eventual scratches from previous step were eliminated. At last, samples were polished in sheets with diamond suspensions of 3 and 1 μm . The surface attack was completed with a 5% nital solution.

2.4.2 Ferritic grain size

Ferritic grain size was assessed accordingly ASTM E112-13 [14] by using the optical Axio Imager M2m microscope from Carl Zeiss, considering the plan defined by the normal and longitudinal (rolling) directions and basic calculations were made by the software Zen, from the same supplier. The average grain size (l , in mm) may be calculated based on the average grain size ASTM (G) by the (Equation 1) [15].

$$G = (-6.644 \times \log_{10} l) - 3.288 \quad (1)$$

2.4.3 X-Ray Diffraction (XRD)

In order to identify the present phases, a 20 x 20 mm sample was prepared exactly like the procedure described for optical microscopy, excluding the nital attack.

XRD was carried out in an Empyrean model, from PANanalytical, using tension equal to 40kV and current of 40 mA. As radiation source, cobalt with wave lengths of $K\alpha_1$ and $K\alpha_2$ of 1.7890×10^{-10} m e 1.7929×10^{-10} m, respectively, was used to avoid the fluorescent effect of the iron [16]. The final diagram was compared to the Inorganic Crystal Structure Database (ICSD). The scanning range (2θ) was between 20° and 110° with steps of 0.026° per position and 46.67 (seconds per step).

2.5 Mechanical tests

2.5.1 Tensile test

Tensile test was performed at room temperature in a Zwick/Roell machine, model Z 250 kN, accordingly to

ASTM A370 [17], with blanks sampled from 3 directions: longitudinal (parallel to rolling), transversal (perpendicular to rolling) and diagonal (45° in relation to rolling direction). Testing samples were machined in a ROMI D800 machining station and remaining burr removed by manual grinding with a soft sandpaper to remove potential spots of stress concentration. Figure 2 presents a schematic drawing of the samples tested as per the ASTM A370 standard [17], including its dimensions.

The main parameters, complying to ASTM A370, were [17]:

- Tensile rate at linear region: 6 MPa/s
- Deformation rate at the yield point: $6.25 \times \%G / \text{min} = 6.25 \times 50 / 100 = 3.125 \text{ mm/min}$
- Deformation rate at the plastic region: $40 \times \%G / \text{min} = 40 \times 50 / 100 = 20 \text{ mm/min}$

2.5.2 Vickers hardness test

Hardness testing was performed at room temperature in a Zwick ZHU250-CLA model with the HVM-G software, accordingly to ISO 6507-1 [18]. Indentation was made with a 136° -pyramidal diamond tip, 5kgf load for 10 seconds.

The results, expressed in kgf/mm^2 , may be given by Equation 2, where F refers to the testing load (in kgf) and d , to the average length of the diagonal indentation of the diamond tip onto the surface (in mm) [19].

$$HV = 1.8544 \frac{F}{d^2} \quad (2)$$

2.5.3 Bending test

Testing samples were machined in a ROMI D800 machining station and remaining burr removed by manual grinding with a soft sandpaper to remove potential spots of stress concentration.

Bending test was performed at room temperature in a Instron / EMIC model 23-300, accordingly to ASTM E290 [20] aiming a final radius close to zero (bend-and-flatten test),

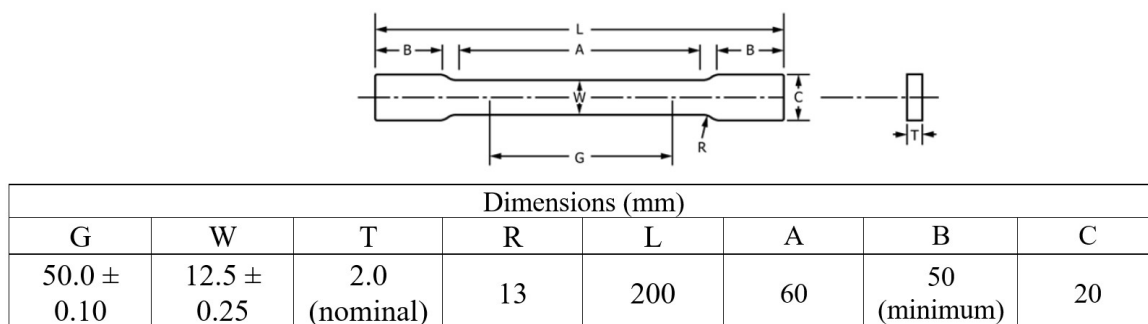


Figure 2. Schematic detailing of tensile testing sample as per ASTM A370 [17].

even more severe than the minimum mandrel radius defined in the standard EN10149-2 [21]. Blanks were selected from both longitudinal and transversal and the acceptance criteria was the absence of cracks in the bending area.

2.5.4 Hole expansion test

Hole expansion testing may be used to assess the material formability and was performed accordingly ISO 16630 [22] in an Erichsen machine model 148/20, with square sample blanks (100 x 100 mm) with a 10 mm-diameter hole in its center.

Initially, internal diameter is measured in both vertical and horizontal directions and the average value calculated. During the test, a 60°-conical tip is forced thru the holes with a constant load of 30 N until a crack may be visible throughout the entire thickness. At this point, the test is stopped, the final diameter of the hole is measured again in both directions and the average value calculated to be compared to the initial one [22]. For statistical purposes, 5 samples were tested, and the maximum and minimum expansion values were excluded, being the result given as the average of the 3 remaining valid measurements.

This limiting criterion is usually referred to as hole expansion ratio (HER) translates itself into Equation 3 [23,24].

$$HER = 100 \times \frac{d_f - d_0}{d_0} [\%] \quad (3)$$

Where d_f and d_0 are the final and the initial diameter of the center hole.

3 Results and discussions

3.1 Microstructural predictions

The resulting microstructure strongly depends on the carbon and nitrogen contents and whether the precipitate

can be dissolved or not. While titanium nitride is virtually insoluble, species such as titanium and niobium carbides or carbonitrides require further investigation to define their solubility. In the reheating phase of rolling process, soaking temperatures between 1100 °C and 1250 °C are typically applied to dissolve niobium and titanium carbide precipitates [25].

The ThermoCalc simulation was divided into steps for didactical purposes. Figure 3A presents the iron-enriched phases of a typical S700MC grade, showing the liquidus line and the formation of both face and body centered cubic phases. Following the carbon-cementite diagram, it may be deduced that for this system that solidification starts at 1514 °C with the formation of a ferrite- δ (BCC) and finishes at 1475 °C. From this point on until 1435 °C, ferrite- δ (BCC) transforms into austenite- γ (CFC) which remains until 854 °C, when ferrite- α (BCC) and Fe₃C starts to form until its full transformation at 672 °C.

Meanwhile, Figure 3B presents the precipitated phases in which should be noticed the formation of FCC phases FCC_A1#2 e FCC_A1#3 and the above-mentioned cementite.

By detailing the FCC_A1#3 phase (Figure 4) it is possible to identify a higher content of titanium, nitrogen and carbon, referred as a solid solution of nitrides and carbides and generally mentioned as Ti(C,N). This forms at 1511 °C, i.e., during steel solidification and way higher than usual reheating temperatures as previously mentioned.

Finally, the FCC_A1#2 phase (Figure 5) presents a higher content of titanium, niobium and carbon, referred as a solid solution of carbides and generally mentioned as (Ti, Nb)C. This forms at 1256 °C, which means this should be the minimum reheating temperature to assure the full dissolution of such carbides.

3.2 CCT and TTT diagrams

Considering the rolling speed (12 m/s), the length of run out table (106 m) and the difference between finishing

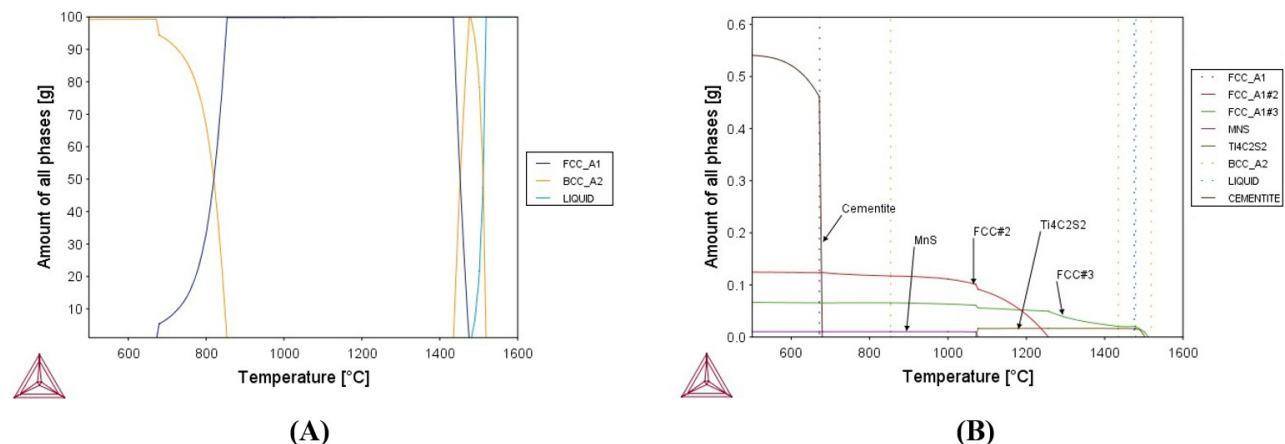


Figure 3. Iron-enriched (A) and precipitated phases (B) simulation by ThermoCalc.

mill exit and the coiling temperature, one may calculate a cooling rate of the strip of 37,4 °C. In accord to the CCT and TTT diagrams (Figure 6), the coiling temperature is still above the bainite formation temperature while the short cooling time prevents the pearlite formation. So, the final microstructure is expected to be a fully ferritic one what shall be confirmed by further analysis in this paper.

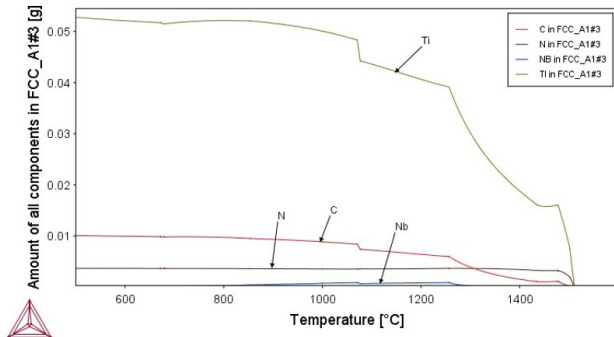


Figure 4. Detail of FCC_A1#3 precipitated phase simulation by ThermoCalc.

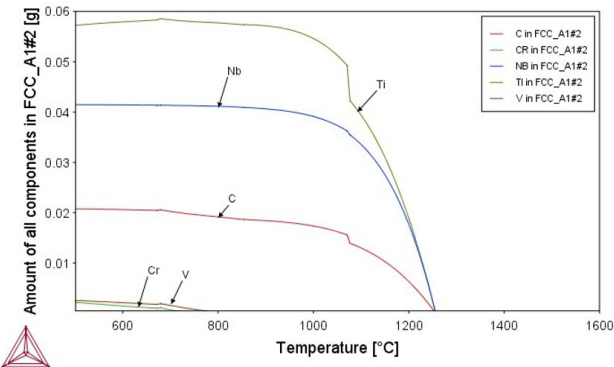


Figure 5. Detail of FCC_A1#2 precipitated phases simulation by ThermoCalc.

3.3 Microstructural characterization

3.3.1 Optical and scanning electronic microscopy

The Figure 7 refers to optical microscopy of sampled coil and suggests a fully ferritic matrix plus elongated carbides and some yellow cuboidal precipitates highlighted in by the arrows (Figure 7A). The precipitate in evidence in Figure 7B was analyzed by scanning electronic microscopy (Figure 8B), confirming the ferritic matrix while further investigation by EDS reveals a composition enriched with titanium and nitrogen, confirming the existence of phase FCC_A1#3 predicted in the item 3.1.

These results comply with literature that reports TiN as golden-yellow cuboidal precipitates [10]. In the middle of the precipitate, there is an enriched phase with aluminum and oxygen, which may be related to some inclusion originated in the steel shop during refining process and also be a preferential site for nucleation of such precipitates.

Further EDS (Figure 9) investigation around the precipitates reveals a titanium and niobium enriched phase, and some precipitates of high iron content which confirms the presence of phase FCC_A1#2 and cementite (Fe₃C) predicted in the item 3.1.

3.3.2 Ferrite grain size

The ferrite grain size was calculated by the planimetric method based on the 3 images presented in Figure 10 while the Table 2 presents the statistical treatment by the ferrite grain size calculation.

Despite only 3 measurements, the relative precision found was 5,37%, lower than the acceptance criteria (10%) defined in the standard which validates the measurements. A grain size ASTM of 12 equals an average diameter of 4.86 μm [15] or, if considering the actual grain size (ASTM = 11.8) and applying Equation 1, 5.18 μm.

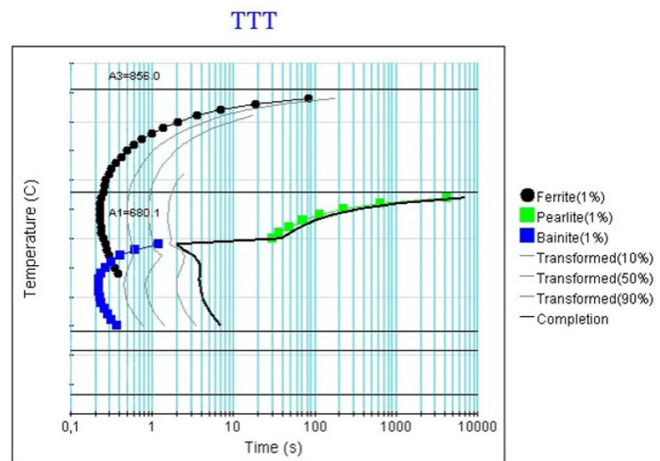
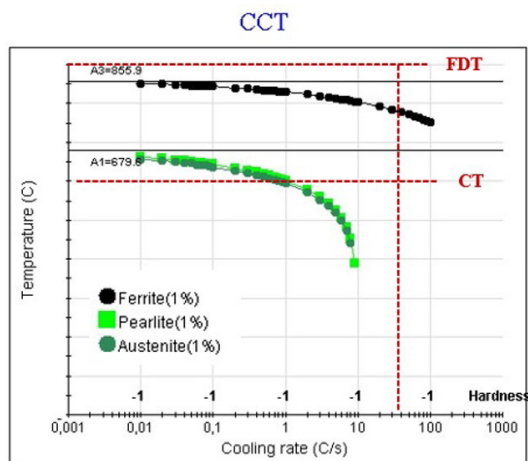


Figure 6. CCT and TTT diagrams simulated by JMatPro.

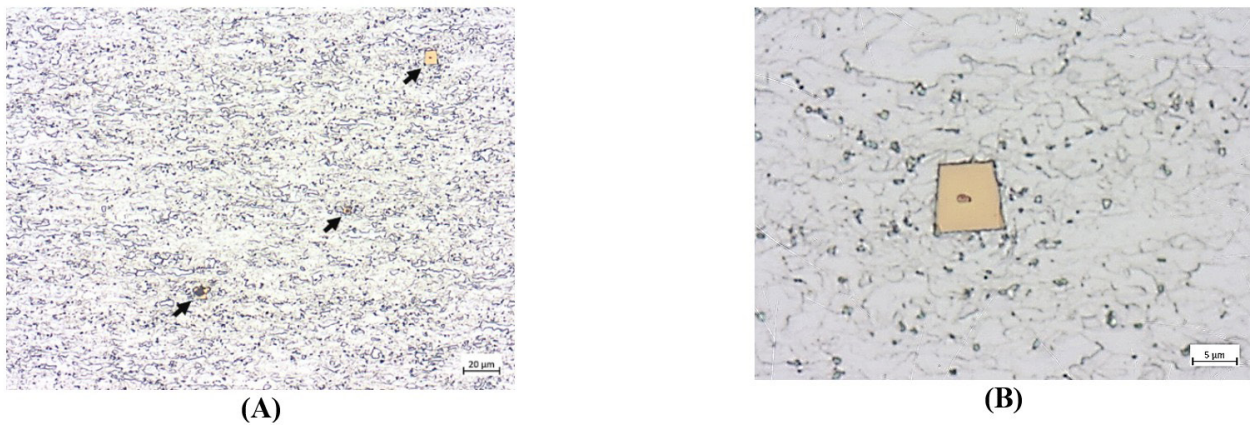


Figure 7. Optical microscopy showing a fully ferritic matrix and precipitates with magnification of 200x (A) and 1000x (B).

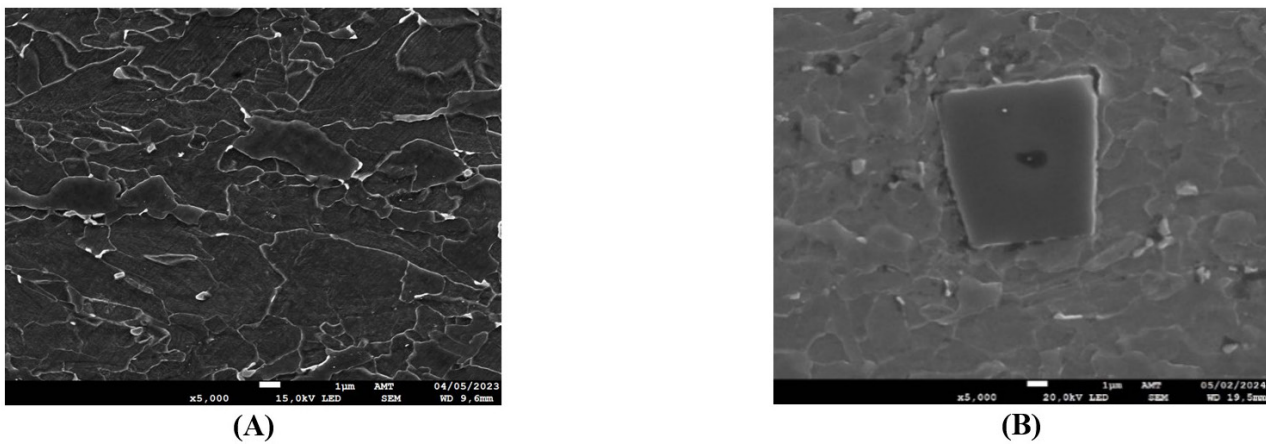


Figure 8. SEM images showing a fully ferritic matrix (A) and precipitates (B). Magnifying: 5000 x

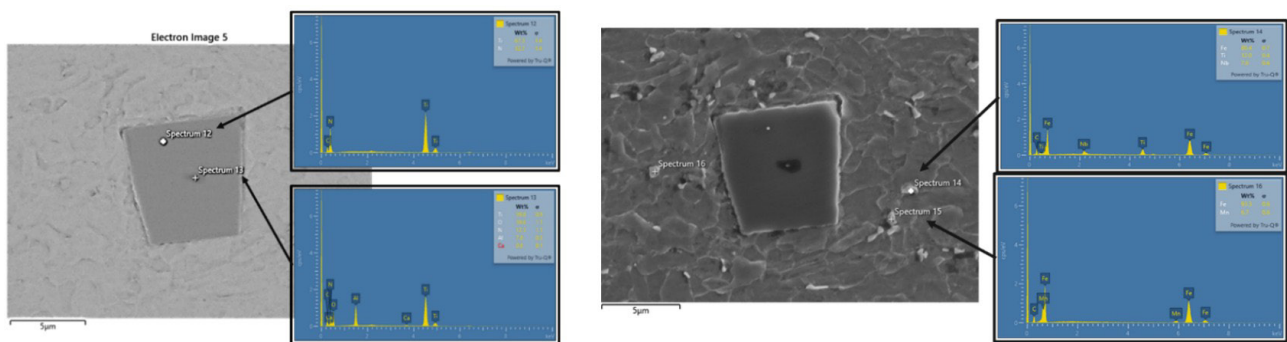


Figure 9. EDS analysis of cuboidal precipitate highlighted Figure 6E revealing a composition enriched with titanium and nitrogen (spectrum 12) and phases enriched in niobium and titanium (spectrum 14) and iron (spectrum 15).

Table 2. Statistical treatment for the planimetric method

Average Grain Size ASTM	Standard Deviation	Confidence interval (95%)	Relative Precision (%)	Number of Grains	Average grain size ASTM Exact
12.0	0.087	0.636	5.374	1997	11.8

3.3.3 X-Ray diffraction

The diffractogram (Figure 11) presented very good correlation to card 98-063-1729 from ICSD corresponding to ferrite- α and no other phase was found, considering the detection limits of the technique [16]. Also, it is very clear the presence of the characteristic peaks from plans (011), (112) and (002).

Table 3 summarizes the main information from ICSD card 98-063-1729 which corresponds to BCC ferrite- α .

The difference in the relative intensity of the peaks experimentally obtained and the values in the ICSD card may be related to a light texture which needs further investigation.

3.4 Mechanical properties

3.4.1 Tension test results

The Table 4 presents the main results from tensile testing in the sample while Figure 12 corresponds to the actual stress-strain curves in all 3 directions.

Considering the yield and tensile strength and the total elongation until fracture in the longitudinal direction, the tested material would meet all requirements for high strength applications for cold forming such as S650MC and S700MC [21].

3.4.2 Vickers hardness results

Hardness measurements are presented an average value of (269.67 ± 1.53) HV or approximately 255 HBW [24]. As a reference, martensitic grades for wear resistant plates may be found in the market with harness values between 370 and 530 HBW [26].

3.4.3 Bending test results

Bending may be defined as a process where a straight length is transformed into a curved length; the fibers on the outer (convex) surface of the bend are stretched, inducing tensile stresses. These tests are used to evaluate the ductility of materials or welded joints during bending [27,28]. Bent samples are presented in Figure 13. Using EN10149-2 [21]

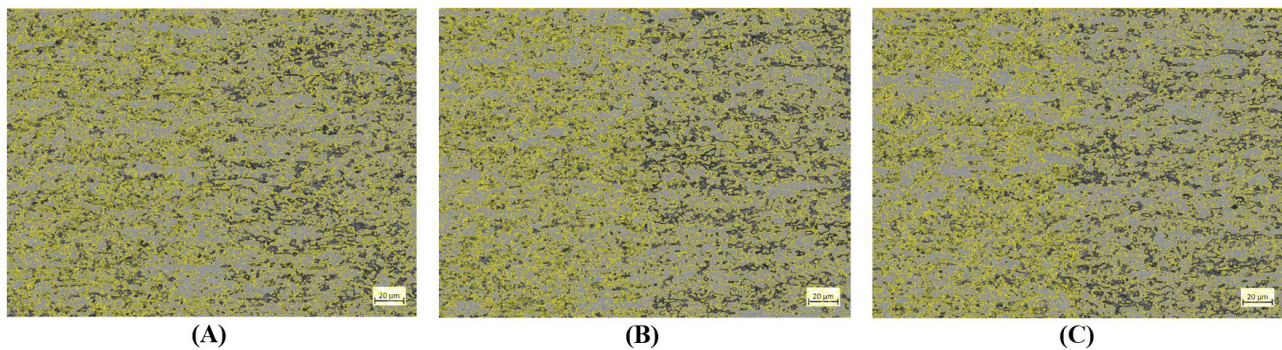


Figure 10. Planimetric method for calculation of ferritic grain size.

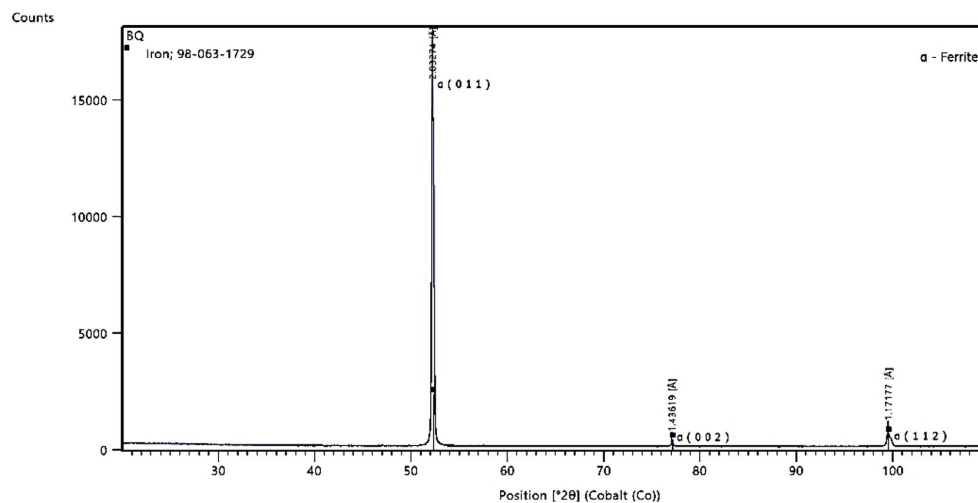


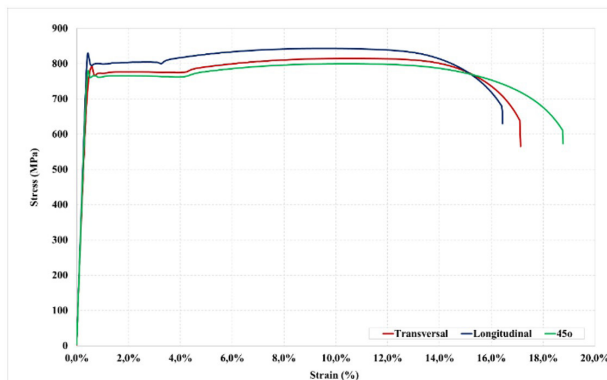
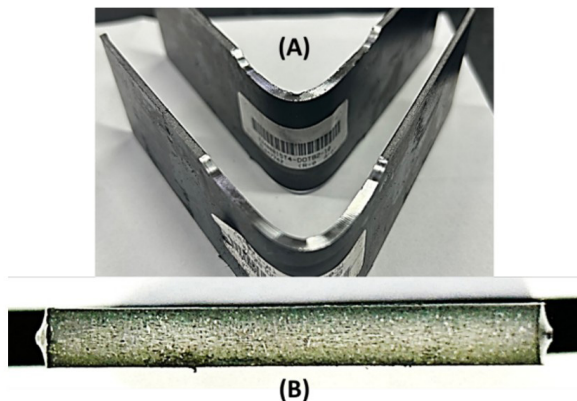
Figure 11. X-Ray diffractogram experimentally obtained corresponding to ferrite- α as per ICSD card 98-063-1729.

Table 3. Main data from ICSD card 98-063-1729

Peak	h	k	l	d [nm]	2 θ [°]	I [%]
1	0	1	1	0.202728	52.365	100.0
2	0	0	2	0.143350	77.218	13.6
3	1	1	2	0.117045	99.679	24.3

Table 4. Main results from tensile testing

Direction	Yield strength (MPa)	Tensile strength (MPa)	Elasticity modulus (GPa)	Total elongation (%)	Uniform Elongation (%)
Longitudinal	790	815	216	17.1	10.36
Transversal	795	843	219	16.4	9.11
Diagonal	761	799	214	18.8	9.99

**Figure 12.** Stress-strain curves for sample tested in 3 directions.**Figure 13.** Testing samples during intermediate step (A) and full bending (B) with no visible cracks.

as a reference, the mandril diameter should correspond to 2 times the nominal thickness of the tested material. Figure 13B shows the tested sample bent up to a radius close to zero (bend-and-flatten test), in a more critical situation than the one established in standard. Since no cracks were found after the testing, the material would be suitable for cold forming applications [20].

3.4.4 Hole expansion test results

Cracking during flanging operations is the major restriction in the use of an advanced high strength steels and a good stretch-flangeability is an essential property for forming complex press formed parts such as chassis and suspension arms [23,29].

To evaluate the flanging capacity, the Hole Expansion Ratio (HER) test was used, using a conical head punch to promote the expansion of the diameter hole until a passing cracking is detected.

The HER is not an intrinsic property of a given material and depends on punch geometry, the hole preparation (laser cutting, machining, or punching), the mechanical properties of the material and its microstructure [23,30]. The 60°-conical punch is the geometry established in the ISO 16630 standard. However, other geometries such as hemispherical and flat-bottom punches may also be used for researching purposes [22,23,30].

The sequence in Figure 14 presents the actual aspect of the samples after punching, indicating the passing cracks as the failure condition. The initial and final dimensions of the tested samples are presented in Table 5. The values from samples 1 and 3 correspond to maximum and minimum values and shall be discarded for statistical purposes. So, hole expansion for the tested material is equal to $48,6\% \pm 2,1\%$.

Considering the mechanical properties presented in item 3.4.1, this result is similar to those obtained for Dual Phase 980 and 1180 grades verified in the literature [23,31,32].

It has been reported that TiN inclusions and cementite act as void nucleation locations during stretching and the precipitation strengthening with small, coherent, and homogeneously distribute particles within the grain can improve resistance and reduce the number of nucleation sites, leading to better ductility. Also, higher HER can be obtained in equiaxed single-phase ferritic microstructure [23].

In the case of Dual Phase (DP) and Complex Phase (CP) steels, the hardness difference between the hard and

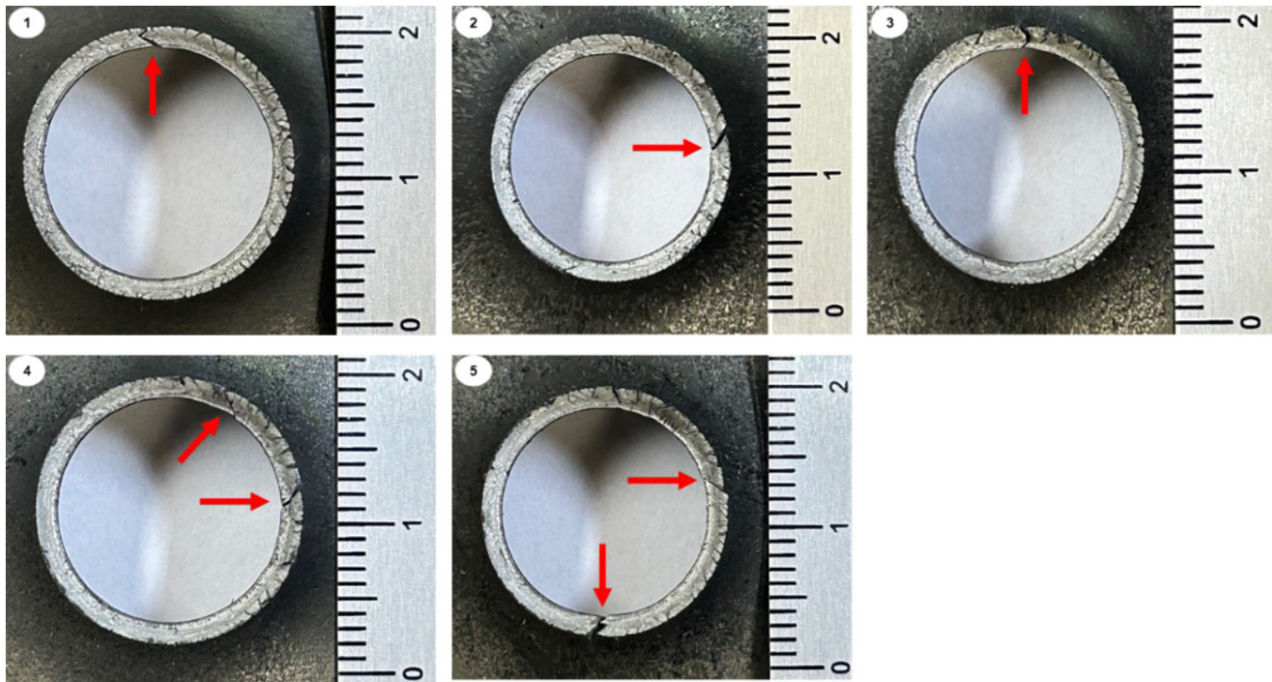


Figure 14. Hole expansion samples after punching. The red arrows indicate the passing cracks.

Table 5. Hole diameter measured before and after expansion testing

Id. Sample	Initial Diameter (mm)			Final Diameter (mm)			HER
	Transv.	Long.	Aver.	Transv.	Long.	Aver.	
1	10.02	10.02	10.02	15.79	15.77	15.78	57.5%
2	10.01	10.02	10.02	15.02	15.10	15.06	50.4%
3	10.00	10.02	10.01	14.07	14.09	14.08	40.7%
4	10.01	10.02	10.02	14.91	14.99	14.95	49.3%
5	10.01	10.02	10.02	14.62	14.68	14.65	46.3%

soft phases results in higher strain localization in the ferrite phase and inferior HER. When tested in the same conditions, samples of CP steels comprising a mixture of ferrite, bainite and tempered martensite may show improved HER when compared to DP steels with high carbon martensite and ferrite because of the smaller hardness difference between the phases [23,32]. The number of martensite colonies per unit area reflects the homogeneity of the microstructure, and it is well established that more homogeneous microstructures have better HER and sheared-edge formability properties [32]. As a reference, multiphase steels containing ferrite, bainite and martensite such as Euronorm HDT780C grade CP800 may reach HER over 100%, depending on the method of preparation of the hole [30].

4 Conclusions

Microstructure assessed by X-ray diffraction and both optical and scanning electronic microscopy of the tested

samples was coherent to offline simulations with a final fully ferritic matrix with elongated carbides, cuboidal TiN precipitates, Fe_3C plus titanium and niobium enriched carbides. This finding is in total accordance with the microstructural predictions performed via ThermoCalc.

Inhibition of grain growth due to precipitates and high reduction from slab up to the strip resulted in refined grains around $5 \mu m$ in a poorly recrystallized matrix, predominating substructured grains with low angle and middle angle sub-grain boundaries.

Considering the yield (790MPa) and tensile strength (815 MPa), total elongation until fracture (17,1%) in the longitudinal direction and the absence of cracks after bending, the tested material would meet all requirements for high strength applications for cold forming such as EN1019-2 S650MC and S700MC. As an additional test, hole expansion for the tested material is equal to 48,6% and results are similar to those obtained for DP grades.

5 Next steps

After this initial characterization, further evaluations will involve studies on the recrystallization (static and dynamic) phenomena and comparisons to actual rolling conditions to improve the accuracy of the deformation resistance calculation model, operational stability, and thickness performance for thin hot rolled Nb and Ti microalloyed steel strips.

Acknowledgements

The author would like to thank Wagner, Ana, Ligia and all the crew from the Mechanical Testing Laboratory from ArcelorMittal Tubarão at Serra (Espírito Santo, Brazil), and the researchers from ArcelorMittal R&D Brazil, specially Joelma, Luciana and Lillian, for all their support during the analysis.

References

- 1 Ma J-L, Chan T-M, Young B. Cold-formed high strength steel tubular beam-columns. *Engineering Structures*. 2021;230:111618.
- 2 Yin F, Wang J, Yang L, Kang N, Elliott F. Testing and design of cold-formed high strength steel square hollow section columns. *Journal of Constructional Steel Research*. 2024;213:108394.
- 3 Senuma T. Physical metallurgy of modern high strength steel sheets. *ISIJ International*. 2001;41(6):520-532.
- 4 Bracke L, De Wispelaere Ahmed NH, Gungor O. S700MC/Grade 100 in heavy gauges: industrialisation at ArcelorMittal Europe. *Revue de Métallurgie*. 2011;108(6):323-330.
- 5 Porto R, Souza MV, Mohallem JADSS, Storch BT, Silva Murad BB, Henriques BR et al Desenvolvimento do aço laminado a quente para atender aos requisitos grau S700 da norma EN10149 na arcelormittal tubarão. In: 72 Congresso Anual da ABM. São Paulo: ABM; 2017. pp. 2064-2073.
- 6 Oktay S, Di Nunzio PE, Sesen MK. Investigation of the effect of isothermal heat treatments on mechanical properties of thermo-mechanically rolled S700MC steel grade. *Acta Metallurgica Slovaca*. 2020;26(1):11-16.
- 7 Kaisheng L, Shao J, Yao C, Pan J, Xie S, Chen D, et al. Effect of Nb-Ti microalloyed steel precipitation behavior on hot rolling strip shape and FEM simulation. *Materials (Basel)*. 2024;17(651).
- 8 Hancock GJ. Cold-formed steel structures. *Journal of Constructional Steel Research*. 2003;59(4):473-487.
- 9 Ostwald P, Muñoz J. *Manufacturing Processes and Systems*. 9th ed. New Jersey: John Wiley and Sons, 1997.
- 10 Harshad B. *Theory of Transformations in Steels*. Boca Raton, Florida: CRC Press; 2021.
- 11 Solis-Bravo GM, Merwin M, Garcia I. Impact of precipitate morphology on the dissolution and grain-coarsening behavior of a Ti-Nb microalloyed linepipe steel. *Metals*. 2020;10(89):89.
- 12 Bleck W, Ratte E. Fundamentals of cold formable HSLA steels. In: *International Symposium on Niobium Microalloyed Sheet Steel for Automotive Application*. The Minerals, Metals & Materials Society (TMS); 2006. pp. 551-564.
- 13 Poliak EI. Dynamic recrystallization control in hot rolling. *Procedia Manufacturing*. 2020;50:362-367.
- 14 Goldstein J, Newbury DE, Michael JR, Ritchie NWM, Scott JHJ, Joy DC. *Scanning Electron Microscopy and X-Ray Microanalysis*. 4th ed. New York: Springer; 2018.
- 15 American Society for Testing and Materials. ASTM E112: Standard Test Methods for Determining Average Grain Size. West Conshohocken: American Society for Testing and Materials (ASTM); 2021.
- 16 Cullity BD. *Elements of X-ray diffraction*. 2nd ed. Boston: Addison-Wesley Company; 1978.
- 17 American Society for Testing and Materials. ASTM A370-22: Standard Test Methods and Definitions for Mechanical Testing of Steel Products. Local: West Conshohocken: American Society for Testing and Materials; 2022.
- 18 International Organization for Standardization, ISO 6507-1: *Metallic Materials - Vickers Hardness Test*. Geneva: International Organization for Standardization (ISO); 2018.
- 19 De Souza SA. *Ensaio Mecânicos de Materiais Metálicos*. 5. ed. São Paulo: Blucher; 1989.
- 20 American Society for Testing and Materials, ASTM E290: Standard Test Methods for Bending Testing of Material and Ductility. West Conshohocken: American Society for Testing and Materials (ASTM); 2022.
- 21 The British Standards Institute. EN10149-2: Hot Rolled Flat Products Made of High Yield Strength Steels for Cold Forming - Part 2. London: The British Standards Institute; 2013.

- 22 International Organization for Standardization (ISO), ISO 16630: Metallic Materials — Sheet and Strip — Hole Expanding Test. Geneva: International Organization for Standardization; 2017.
- 23 Paul SK. A critical review on hole expansion ratio. *Materialia*. 2020;9:100566.
- 24 Hance BM. Practical application of the hole expansion test. *SAE International Journal of Engines*. 2017;10(2):247-257.
- 25 Weibel J, Mohrbacher H, Detemple E, Britz D, Mucklich F. Quantitative analysis of mixed niobium-titanium carbonitride solubility in HSLA steels based on atom probe tomography and electrical resistivity measurements. *Journal of Materials Research and Technology*. 2022;18:2048-2063.
- 26 ArcelorMittal. Industeel Relia [Internet]. 2018 [cited 2024 July 18]. Available at: <https://industeel.arcelormittal.com/wp-content/uploads/2021/03/DS-WEAR-RELIA-Rev-042018.pdf>.
- 27 Davis JR. *Metals Handbook*. 2nd ed. Russel Township: ASM International; 1998.
- 28 Dieter GE. *Mechanical Metallurgy*. Singapore: McGraw-Hill; 1988.
- 29 Pathak N, Butcher C, Worswick MJ, Bellhouse E, Gao J. Damage evolution in complex-phase and dual-phase steels during edge stretching. *Materials (Basel)*. 2017;10(346):346.
- 30 Jesus HS, Ferreira FGN, Ferreira JL, Mohallem J, Souza WM, Pedrini RH, et al. Evaluation of the flange stretching capability of a 780 MPa class multiphase advanced high strength steel. *Tecnologica em Metalurgia, Materiais e Mineração*. 2024;21:e2997.
- 31 Paul SK, Mukherjee M, Kundu S, Chandra S. Prediction of hole expansion ratio for automotive grade steels. *Computational Materials Science*. 2014;89:189-197.
- 32 Terrazas OR, Findley KO, Van Tyne CJ. Influence of martensite morphology on sheared-edge formability of dual-phase steels. *ISIJ International*. 2017;57(5):937-944.

Received: 18 July 2024

Accepted: 6 Feb 2025

Editor-in-charge:

Sabrina Arcaro 